PCCP

PAPER

Check for updates

DFT–ReaxFF hybrid molecular dynamics investigation of the decomposition effects of localized high-concentration electrolyte in lithium metal batteries: LiFSI/DME/TFEO†

Yiming Lu, Qintao Sun, Yue Liu,* Peiping Yu, Yanyan Zhang, Jiachen Lu, Haochen Huang, [ID] Hao Yang [ID] * and Tao Cheng [ID] *

Due to its low electrochemical potential and high theoretical specific energy, lithium-metal batteries (LMBs) have been considered as a promising advanced energy storage system for portable applications such as electric vehicles (EVs). However, the uncontrolled growth of lithium dendrites during cycling has remained a challenge. By utilizing an inert solvent to "dilute" the high concentration electrolytes, the concept of localized high-concentration electrolytes (LHCEs) has recently been demostrated as an effective solution to enable the dendrite-free cycling of LMBs. In this work, we investigated the reactions of 2 M lithium bis(fluorosulfonyl)imide (LiFSI) in a mixture of dimethoxyethane (DME)/tris(2,2,2-trifluoroethyl) orthoformate (TFEO) electrolyte at a Li metal anode. The SEI formation mechanism is investigated using a hybrid *ab initio* and reactive force field (HAIR) method. The 1n reactive HAIR trajectory reveals the important initial reduction reactions of LiFSI, TFEO, and DME. Particularly, both FSI anions and TFEO decompose quickly to release a considerable amount of F^-, which leads to a LiF-rich SEI inorganic inner layer (IIL). Furthermore, TFEO produces a significant amount of unsaturated carbon products, such as thiophene, which can potentially increase the conductivity of SEI to increase the battery performance. Meanwhile, XPS analysis is utilized to further investigate the evolution of the atomic environment in SEI. Future designs of better electrolytes can be greatly aided by these results.

1 Introduction

With the rapid development of renewable technologies, portable applications have increasing requirements for energy storage systems. Lithium (Li) metal anodes offer the highest theoretical capacity (3860 mA h g^{-1}) and lowest electrochemical potential (-3.04 V *vs.* standard hydrogen electrode) among all anode materials for lithium batteries. As a result of their outstanding performance, the LMBs have recently gained a lot of attention.[1–6] While LMBs are gaining empirical support, commercial applications are still in their infancy. Particularly, safety risks caused by flammable liquid electrolytes and short circuits due to lithium dendrite formation during cell cycling have so far prevented the use of lithium metal in commercial batteries. During charge and discharge cycles, the lithium dendrite growing can puncture the

Institute of Functional Nano & Soft Materials (FUNSOM), Jiangsu Key Laboratory, for Carbon-Based Functional Materials & Devices, Soochow University, 199, Ren'ai Road, Suzhou, 215123, Jiangsu, P. R. China. E-mail: yliu1992@suda.edu.cn, haoyang@suda.edu.cn, tcheng@suda.edu.cn

† Electronic supplementary information (ESI) available: Simulation model, XPS prediction, and detailed product analysis. See DOI: https://doi.org/10.1039/d2cp02130g

membrane, causing short circuits in batteries. Thus, lithium metal must be protected to achieve a long-cycle life.[6–11]

Significant progress has been made in electrolyte research in recent years by raising the salt concentration in a specific salt–solvent combination to generate high concentration electrolytes (HCEs) or super concentration electrolytes (SCEs). The amount of free solvent molecules in the electrolyte is considerably reduced, while the number of contact ion pairs (CIPs) and aggregates is greatly increased (AGGs).[8,9,11] As a result of the anions' lower lowest unoccupied molecular orbital (LUMO) energy and extensive coordination to Li$^+$, salt anions are reduced prior to solvent molecule reduction and form an anion-derived SEI. When compared to the solvent-derived SEI, this anion-derived SEI has greater ionic conductivity and mechanical strength. HCEs or SCEs, on the other hand, have a number of drawbacks, including low conductivity, high viscosity, and poor wettability between electrode and separator, all of which restrict their commercial applications.[12–15]

One option is to dilute HCEs with diluents to generate locally high-concentration electrolytes (LHCEs), which can successfully lower the electrolyte's viscosity and salt concentration while preserving high-coordination clusters. On the basis of the

high-concentration electrolyte, LHCEs employ free inert solvent molecules as diluents to localize the high-concentration region, ensuring that the original tight ion pairs, ion aggregates, and other solution structures are not diluted by the adjustment.[12,16] The local high-concentration system has lower solution viscosity and greater electrode wettability than the high-concentration system, and it is more likely to be compatible with traditional liquid injection technology for practical application.[15,17–19] Cao *et al.* recently revealed tris(2,2,2-trilfuoroethyl) orthoformate (TFEO) as a suitable electrolyte component for LMBs in their research, which has a high boiling point, high oxidative stability, and low viscosity.[20,21] The TFEO-based electrolyte outperforms traditional carbonate- and ether-based electrolytes in terms of electrochemical performance. However, based on past research, the specific role of the TFEO in the electrolyte is still unknown.

X-Ray photoelectron spectroscopy (XPS) and quantum chemical calculations have been utilized to evaluate SEI in earlier investigations. These characterization methods, on the other hand, did not go into great depth on how TFEO and LiFSI breakdown throughout the SEI's development. We require an immediate technique of illustrating what happened during the chemical reaction. *Ab initio* molecular dynamics (AIMD) simulations have been found to be beneficial in comprehending SEI initial reaction step, but because of the high computational cost, the simulation time scale is limited to tens of picoseconds (ps). Instead, The development of SEI films takes nanoseconds (ns) or longer, which is significantly longer than the tens of picoseconds (ps) reached in conventional AIMD simulation time scales.[22,23] Thus, the simulation time scale of brute force AIMD is insufficient to investigate the generation of SEI film. Another alternative is to use empirical methodologies, such as the reactive force field (Reactive Force Field, ReaxFF) derived from quantum mechanics (QM). ReaxFF is frequently used to describe complex multi-phase chemical processes and has a significantly reduced computational cost. The use of ReaxFF simulation can help to extend the time scale of SEI simulation so that the deep reactions in SEI can be better explored. Although the initial functional form of ReaxFF does not have description of electron,[24] eReaxFF has solved this problem by explicit including electron terms *via* integration of the Atom-condensed Kohn–Sham DFT approximated to second order (ACKS2) charge calculation scheme.[25] Such development significantly facilitates the application of empirical potential in electrochemical reaction. For example, Islam and van Duin demonstrate that eReaxFF can well reproduce important reactions in ethylene carbonate decomposition.[26] More progress on the development of ReaxFF are summarized in a recent review paper[27]

In this study, we used a hybrid *ab initio* and reactive molecule dynamics (HAIR) method, which combines the advantages of AIMD and ReaxFF molecular dynamics. With well-trained force field parameters, ReaxFF MD in HAIR accelerates mass transfer with an accuracy equivalent to QM but at a lower cost, while retaining the AIMD component of the HAIR approach to correctly characterize electrochemical processes.[28–30] Different from the high-concentrated electrolyte (HCE), special attention is paid to a localized high-concentration

electrolyte to investigate the role of diluent. Using HAIR, we investigated the initial reactions of 2 M lithium bis(fluoro-sulfonyl)imide (LiFSI) in a mixture of dimethoxyethane (DME)/tris(2,2,2-trifluoroethyl) orthoformate (TFEO) (2 : 3 by mol) electrolyte with a Li metal anode. The underlying reaction mechanism of SEI formation is then elucidated in a time scale of 1 ns. XPS analyses were carried out to further reveal the SEI components that can be directly compared with the experiment.

2 Methods and models

2.1 Simulation methods

The HAIR scheme employs AIMD and reactive molecular dynamics (RMD) simulations alternatively, which contains 0.5 ps AIMD and 5.0 ps RMD with a 10-time acceleration. In the AIMD part, all of the AIMD simulations are performed using Vienna *ab initio* Simulation Package (VASP) at a version of 5.4.4. Canonical (*NVT*) ensembles are used and the Nosé–Hoover thermostat is set with a damping parameter of 200 fs. For equilibrations, the velocities are scaled to the target temperature every 20 steps. And gamma point of the Brillouin zone with no consideration of symmetry is used during MD simulations. The Perdew–Burke–Ernzerhof (PBE) functional was utilized to characterize the electron exchange and correction energies inside the generalized gradient approximation (GGA). We used the DFT-D3 method with Becke-Jonson damping to calculate the dispersion correction. The projector augmented wave (PAW) approach and a plane wave basis set are used as implemented in VASP. To sample the Brillouin zone integration, we employed a $1 \times 1 \times 1$ Monkhorst-Pack k-point mesh and a 400 eV energy cutoff for plane-wave basis expansion, which facilitates affordable computational cost with accurate prediction based on our benchmark calculation. The partial occupancies for each orbital are set with the first order Methfessel-Paxton scheme in the smearing width of 0.2 eV. The threshold for the self-consistent field's electronic structure convergence was established at 10^{-4} eV. Spin polarization does not have an appreciable effect on the overall energies and is not included in the calculations to reduce computational demands. The time step during AIMD simulations is 1 fs. In the RMD simulation, all of the RMD is conducted with the USER-REAXC package in LAMMPS (12 Dec 2018). The conventional ReaxFF functional form used in this work is proposed in 2008,[31] and the force field parameters are developed by Liu *et al.*[25,26] To obtain good energy conservation, a 0.25 fs time step is used during RMD simulation. The velocities are scaled to the target temperature every 20 steps. For productions, the canonical (*NVT*) ensemble was relaxed by using the Nos–Hoover thermostat with a damping parameter of 50 fs.

In current HAIR scheme, no constraint is applied in the ReaxFF MD part. Therefore, reactions are possible when the simulation switches to RMD part. The benefit is that such a procedure may guarantee a continual reactive trajectory. Although ReaxFF is not as accurate as AIMD in describing electrochemical reactions, the risk is low because the chance of a reaction in ReaxFF at an early stage is low.

This journal is © the Owner Societies 2022

Phys. Chem. Chem. Phys., 2022, **24**, 18684–18690 | **18685**

Using one Intel Xeon Gold 6226R node (32 cores 16 × 2.9 GHz), a 1 ns HAIR simulation can be completed in less than one week, which is comparable to ~100 days of brute force AIMD simulation. Although greater time scales are more desirable, HAIR simulation cannot reach microseconds because it still relies on AIMD for 1% to 10%.

2.2 Simulation models

A 6-layer (3 × 3) supercell slab was used to model the Li-metal anode, with two of the bottom layers fixed (see Fig. S1, ESI†) and the most stable Li (100) surface. The number of DME and TFEO molecules in the simulation box was 2 and 3, respectively. Two LiFSI salt molecules were sufficient to achieve 1 M LiFSI/DME/TFEO electrolyte systems. Periodic boundary conditions are used in this work and the cell is 10.5 × 10.5 × 26.5 Å approximately.

2.3 XPS analysis

The calculated method of core-level energy is implemented in VASP at PBE-D3 level.[32] There are two methods to calculate the core-level energy – the initial and final state approximation, in VASP. The initial state approximation is based on Kohn–Sham's (K.S.) eigenvalues of the core state after self-consistent calculation of the valence charge density, while the final state approximation requires electrons to be removed from the core and put into the valence state.[33] Due to the reliability in reproducing the relative binding energy change as measured experimentally, we select the initial state method to calculate the core level of the element and compared it with the corresponding binding energy in the experiment.[34] To simulate the intensity of XPS figures, a thousand AIMD trajectories after the SEI formed were used to calculate the core level energy.[35] All of the calculated core level energies are classified by the element, and the histograms of frequency distribution whose group distance is 0.1 eV are drawn according to the core level energy values, and the XPS spectrum is based on the histograms. Peak fitting is based on peak location and structures information in trajectories.

3 Results

The S–F bond is broken first at 0.5 ps (Fig. 1a), followed by the S–N bond at 5.95 ps (Fig. 1b) in LiTFSI. Similarly, the F atom is steadily vanishing. It was degraded into NSO_2, NSO, SO_2, and other fragments by 11.5 ps (Fig. 1c). The inorganic layer SEI is formed by the shed F, O, and surface Li atoms, which combine to create LiF and Li_2O. At 17.0 ps (Fig. 1d), fragment NSO emits one O, forming NS, which might trigger the breakdown of the initial TFEO in the following reaction. At 44.0 ps (Fig. 1e), NS reacts with NSO_2 to produce the unstable $N_2S_2O_2$ intermediate. S breaks off at 44.5 ps (Fig. 1f), producing N_2SO_2, which further decomposes into SO and N_2S. Finally, at 49.6 ps (Fig. 1g), N_2S detaches from the end group S, forming N_2 (Fig. 1h). The S that was lost during the entire process is free in the reaction system and can take part in the following reaction.

The diverse chemical environments in the reaction system cause TFEO molecules to decompose in three different ways. Among them, the first and the second are the C–F bonds that preferentially break the end groups, and the third is the
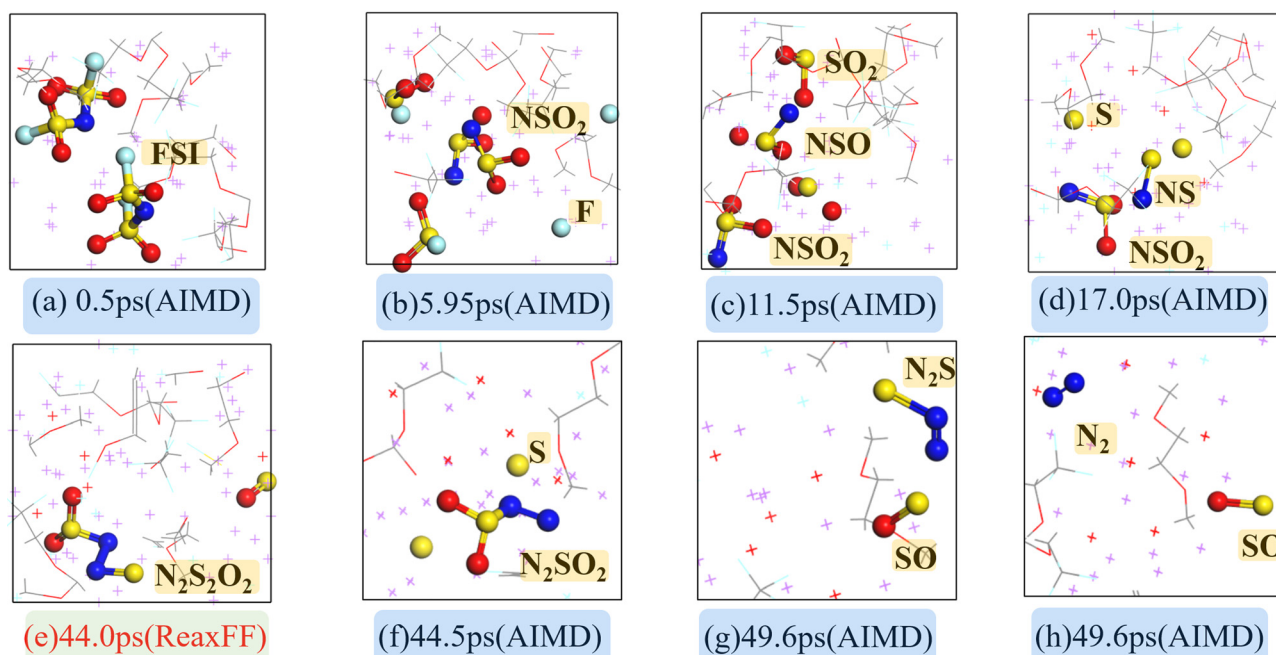

Fig. 1 Sequences of FSI decomposition were obtained from HAIR simulations for the 2 M LiFSI/TFEO/DME electrolyte system between 0 and 50 ps: (a) 0.5 ps, (b) 5.95 ps, (c) 11.5 ps, (d) 17.0 ps, (e) 44.0 ps, (f) 44.5 ps, (g) 49.59 ps and (h) 49.60 ps. The red on green 44.0 ps was observed in ReaxFF MD. The black on blue 0.5 ps, 5.95 ps, 11.5 ps, 17.0 ps, 44.5 ps, 49.59 ps, and 49.60 ps were observed in AIMD simulation. Color code: lithium, purple; oxygen, red; carbon, gray; fluorine, cyan; sulfur, yellow, nitrogen, blue; hydrogen, white.

18686 | *Phys. Chem. Chem. Phys.*, 2022, **24**, 18684–18690

This journal is © the Owner Societies 2022

preferential breakage of the C–O bonds. The initial reaction route is depicted in Fig. 2. The NS fragment acquired from the breakdown of LiFSI works as an initiator to activate the C–F bond of the first TFEO molecule, and the C–F bond is broken at 17.4 ps (Fig. 2a) in the first decomposition pathway. The C–O bond on the branch was weakened as a result of the C–F bond breaking, and it broke at 22.0 ps (Fig. 2b). At this time $(CF_3CH_2O)_2CHO$ and CH_2CF_2 fragments are generated (Fig. 2c). CH_2CF_2 fragments continue to decompose, and finally, CH_2C is formed at 28.3 ps (Fig. 2d). The fallen F and Li in the surrounding environment form LiF, which becomes an important part of inorganic SEI. Then an O–C bond in $(CF_3CH_2O)_2$ CHO is broken at 33.03 ps to generate CF_3CH_2O-CHO (Fig. 2e) and CF_3CH_2O (Fig. 2f). At 33.26 ps, CH_2C attacked the end group of the generated CF_3CH_2OCHO to generate long-chain $CF_3CH_2OCHOCCH_2$, which was unstable and then disconnected at 49.7 ps to generate CH_2CCHO and CF_3CH_2O (Fig. 2g).

The C–F bond is activated and severed at 28.1 ps in the second breakdown pathway because TFEO is in a chemical environment near the surface of the Li metal electrode (Fig. 3a). After about 5 ps (33 ps), the C–O bond is broken, generating $(CF_3CH_2O)_2CHO$ and CH_2CF_2 fragments (Fig. 3b). Among them, CH_2CF_2 fragments continue to decompose, and finally, CH_2C is formed at 44.6 ps (Fig. 3c). The fallen F and Li in the surrounding environment form LiF, which becomes an important part of inorganic SEI. At 55.0 ps (Fig. 3d), the C–F bond at one end of $(CF_3CH_2O)_2CHO$ is broken to generate $CF_3CH_2OCHOCCH_2$, which is unstable and continues to decompose to generate CF_3CH_2O, CF_2CH_2, and CHO_2 fragments at 66.3 ps (Fig. 3e). CF_3CH_2O and CF_2CH_2 continue to dehydrogenate respectively

(Fig. 3f). $CFCH_2O$ and CH_2C are generated at 77.3 ps (Fig. 3g) from the decomposition of the above fragments. At 83.0 ps (Fig. 3h), the CCH_2O fragment undergoes a 1,2-hydride shift to generate the $CHCHO$ fragment, which provides more sites for the subsequent ring-forming reaction.

The difference between the third decomposition pathway and the first two is that the path to breaking is the C–O bond firstly, which makes this pathway take place at the latest after the first two pathways have reacted completely. At 126.5 ps (Fig. 4a), the CO bond is broken to generate $(CF_3CH_2O)_2CHO$ and CH_2CF_3 fragments. The CH_2CF_3 fragment continues to decompose, and the CF bond is gradually broken. The shed F ions combine with Li in the surrounding environment to form LiF. At 132.5 ps (Fig. 4b), the F on CH_2CF_3 falls off completely. Next, at 149.0 ps, the C–O bond in $(CF_3CH_2O)_2CHO$ was broken to generate CF_3CH_2O and CF_3CH_2OCHO fragments (Fig. 4c). Then, after 49 ps (198 ps, Fig. 4d), CF_3CH_2OCHO was broken to generate CF_3CH_2O and CHO fragments. The generated CF_3CH_2O fragments are continuously defluorinated to eventually generate fragments to form the next organic ring, such as thiophene.

Subsequently, as depicted in Fig. 5, the CHOS in the reaction system combines with CHCO to form an unstable intermediate $C_3H_2O_2S$ at 407.0 ps (Fig. 5a), which then decomposes to form CHO and C_2 HOS at 407.3 ps (Fig. 5b). As the reaction proceeds, the sulfur in C_2HOS migrates to generate CHCSO at 417.5 ps (Fig. 5c), and this fragment combines with CHCO in the system at 418.0 ps which eventually generates $C_4H_2O_2S$ with a thiophene ring structure (Fig. 5d).

XPS data reveal compounds comprising C, O, and F components in SEI, as well as a comparison between the estimated
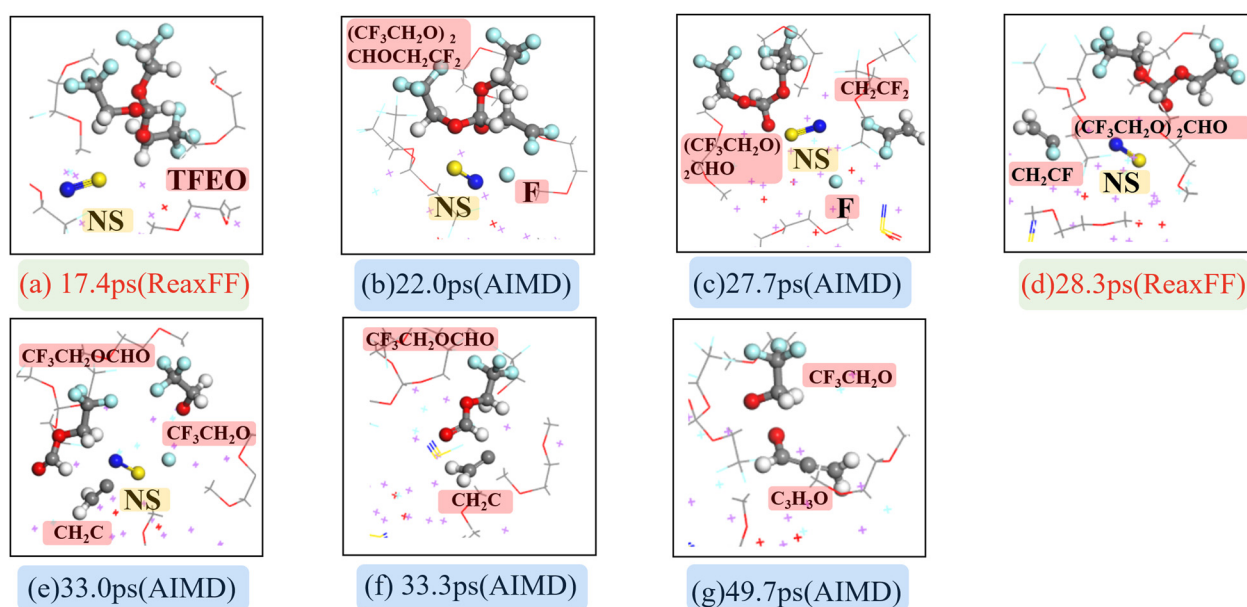

Fig. 2 Sequences of the first TFEO decomposition was obtained from HAIR simulations for the 2 M LiFSI/TFEO/DME electrolyte system: (a) 17.41 ps, (b) 22.04 ps, (c) 27.7 ps, (d) 28.3 ps, (e) 33.03 ps, (f) 33.26 ps, and (g) 33.65 ps. The red on green 17.4 ps and 28.3 ps were observed in ReaxFF MD. The black on blue 22.0 ps, 27.7 ps, 33.0 ps, 33.3 ps, 49.7 ps, and 49.59 ps were observed in the AIMD simulation. Color code: lithium, purple; oxygen, red; carbon, gray; fluorine, cyan; sulfur, yellow; nitrogen, blue; hydrogen, white.
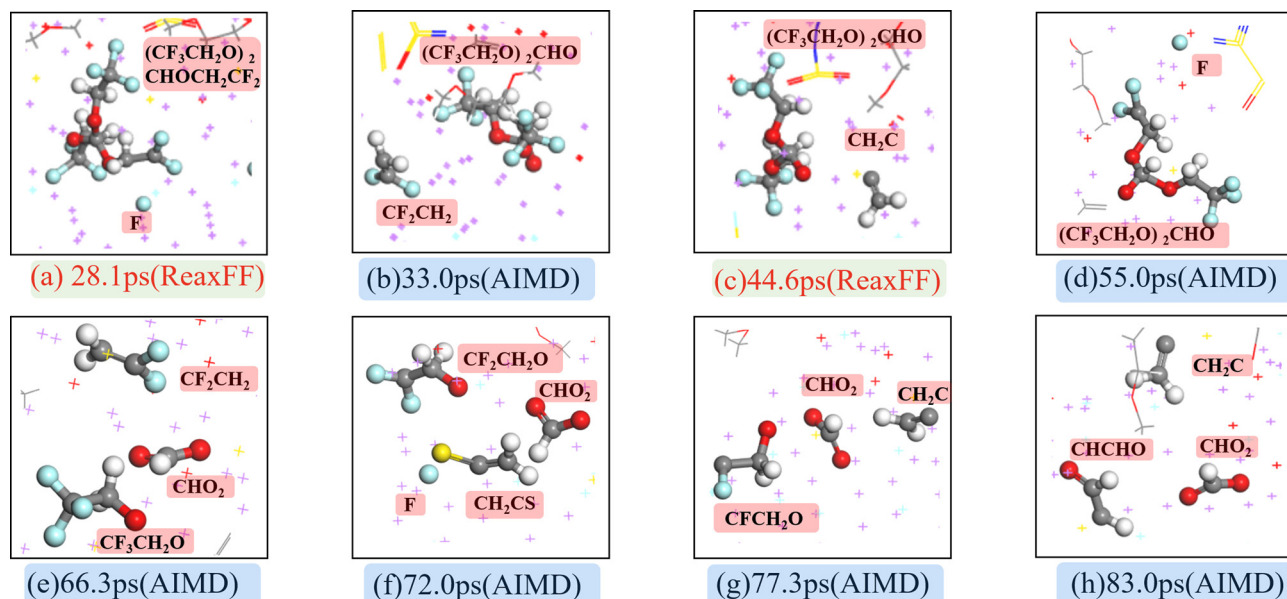
This journal is © the Owner Societies 2022

Phys. Chem. Chem. Phys., 2022, **24**, 18684–18690 | **18687**

Fig. 3   Sequences of the third TFEO decomposition was obtained from HAIR simulations for the 2 M LiFSI/TFEO/DME electrolyte system: (a) 126.5 ps, (b) 132.5 ps, (c) 149.0 ps, and (d)198.0 ps. The red on green 132.5 ps was observed in ReaxFF MD. The black on blue 126.5 ps, 149.0 ps, and 198.0 ps was observed in the AIMD simulation. Color code: lithium, purple; oxygen, red; carbon, gray; fluorine, cyan; sulfur, yellow; nitrogen, blue; hydrogen, white.
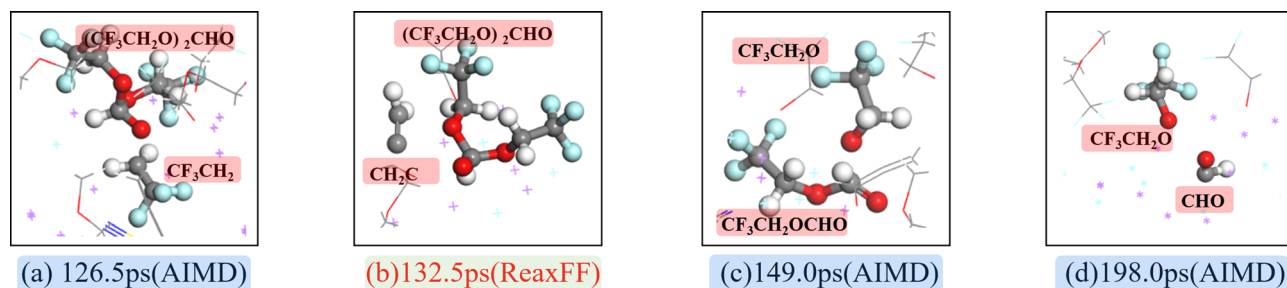

Fig. 4   Sequences of the third TFEO decomposition was obtained from HAIR simulations for the 2 M LiFSI/TFEO/DME electrolyte system: (a) 126.5 ps, (b) 132.5 ps, (c) 149.0 ps, and (d)198.0 ps. The red on green 132.5 ps was observed in ReaxFF MD. The black on blue 126.5 ps, 149.0 ps, and 198.0 ps was observed in the AIMD simulation. Color code: lithium, purple; oxygen, red; carbon, gray; fluorine, cyan; sulfur, yellow; nitrogen, blue; hydrogen, white.
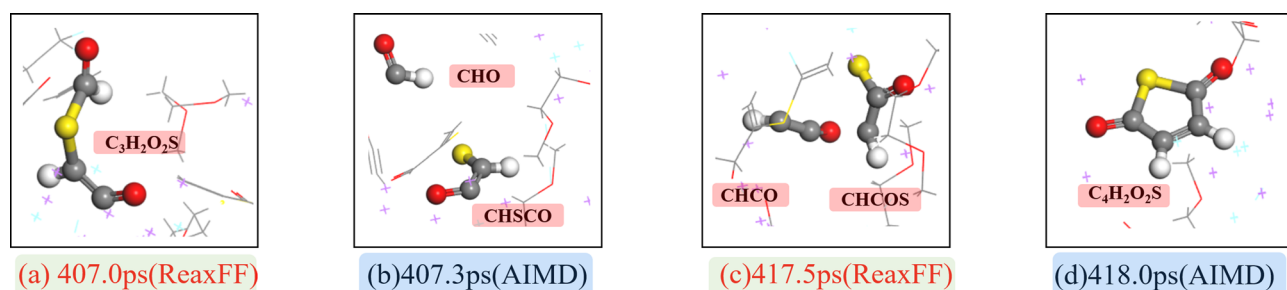

Fig. 5   Sequences of the first thiophene formation was obtained from HAIR simulations for the 2 M LiFSI/TFEO/DME electrolyte system: (a) 407.0 ps, (b) 407.3 ps, (c) 417.5 ps, and (d) 418.0 ps. The red on green 407.0 ps and 417.5 were observed in ReaxFF MD. The black on blue 407.3 ps and 418.0 ps were observed in the AIMD simulation. Color code: lithium, purple; oxygen, red; carbon, gray; fluorine, cyan; sulfur, yellow; nitrogen, blue; hydrogen, white.

and observed binding energy shifts. In this work, the core level shift is predicted from the initial-state (IS) approximation, which involves recalculating the Kohn–Sham eigenvalues of the core states. Although the IS approximation underestimate the absolute values, it is still reliable because the experimental trend can be well-reproduced. From C_{1s} XPS (Fig. 6a), the main
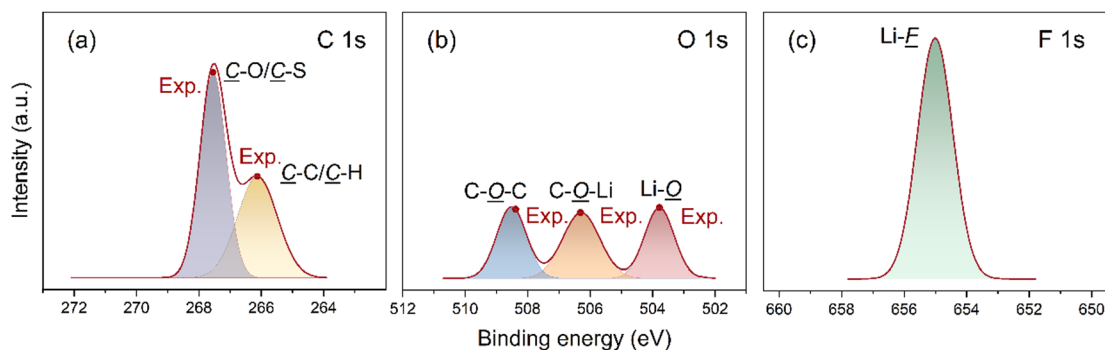
18688 | Phys. Chem. Chem. Phys., 2022, 24, 18684–18690

This journal is © the Owner Societies 2022

Fig. 6 X-ray photoelectron spectroscopy (XPS) of C_{1s}, O_{1s} and F_{1s} of FSI-TFEO-DME (a–c). Experimental binding energy shift to C−C/C−H and Li−O in C_{1s} and O_{1s} respectively as are marked with wine red dots from ref. 20, 21 and 34−37.

components of carbon-based species are C–O/C–S, and from O_{1s} XPS (Fig. 6b), the C–O bond can be divided into the C–O–C bond and C–O–Li spaces, and from S_{2p} (Fig. S2, ESI†), the compounds with C–S bond are C–S–C that is the thiophene and C–S–Li bond. Analysis of the SEI trajectory (Fig. 5d) demonstrates that the C–S–C bond originating from thiophene has the potential to increase the conductivity of SEI, hence enhancing device performance. When combined with the exceptionally stable LiF component in SEI, the S rich SEI reduces the morphology of lithium dendrites and porous lithium metal, hence reducing anode and cathode deterioration. In addition, the Li_2O-containing Li–O bond occurred in O_{1s} XPS. In F_{1s} XPS (Fig. 6c), there is just one Li–F bond left, whereas all C–F and S–F bonds in TFEO and LiFSI are breaking to create LiF with lithium metal anode. Moreover, the binding energy shift value is fitted well with related experimental work,[20,21,34–37] the error between experimental binding energy shift and calculated binding energy shift is less than 0.1 eV.

4 Conclusion

In this work, HAIR technique that hybrids *ab initio* and reactive molecular dynamics is employed to investigate the reduction mechanisms in the initial stage of SEI formation of Li metal anode in a 2 M LiFSI/TFEO/DME electrolyte. Taking TFEO as a diluent forming a local high-concentration electrolytes (LHCE), the electrochemical performance of the lithium metal anode is significantly improved when compared with equivalent high concentration electrolytes (HCE). The salts cannot be dissolved by the TFEO solvent, but they can be dissolved by the DME solvent, which is miscible with TFEO. Thus, DME accommodates salts, while TFEO reduce the interaction between Li^+ and FSI^-. In such an environment, salt, (FSI^-), decomposes more quickly, which sacrificially protects solvent molecules. In addition, the decomposition of TFEO generates a substantial number of unsaturated carbon compounds, such as thiophene, which have the ability to reduce the resistance of SEI and improve battery performance. Furthermore, the presence of oligmers smooth the morphology of lithium dendrites and porous lithium metal when paired with the extremely stable LiF component in SEI, hence greatly preventing anode and cathode degradation. We noticed

that the decomposition of FSI anions is quicker than the dissolution of TFEO, suggesting that an NS fragment might be employed as a trigger to initiate the TFEO decomposition process. By tracing the trajectory of the HAIR simulation, a precise initial reduction process of DME/TFEO is elucidated: the decomposition of TFEO can provide significant amount of F to quickly consume Li forming LiF, which serves as a protective inorganic layer. Recent study has demonstrated that an SEI composition combining both organic and inorganic components is more advantageous to lithium battery performance, and our results support this. XPS analysis is used to further explore the development of SEI morphology, and our simulated results are in accord with experimental observations.

HCE and LHCE provide a number of benefits over traditional electrolytes. Our research provides a new route for the design of electrolyte and increases our understanding of the chemistry in battery interphase. In addition, it presents a way for the practical manufacturing of lithium metal batteries with enhanced safety, high specific energy, and extended cycle life. This study illustrates that the multi-scale simulation reveals the reduction mechanism and morphological evolution of the SEI formation process, offering new insights for the design of future electrolytes.

Author contributions

T. C., Y. L. and H. Y. conceived the project; Y. M. L. and Q. T. S. conducted the calculations with the assistant from P. P. Y; Y. H., Y. Y. Z., J. C. L., and H. C. H. T. C., Y. L. and H. Y. supervised the project; T. C., Y. L., H. Y. and Y. M. L. wrote the paper with comments from all authors.

Conflicts of interest

There are no conflicts to declare.

Acknowledgements

This journal is © the Owner Societies 2022

Phys. Chem. Chem. Phys., 2022, **24**, 18684–18690 | **18689**

Notes and references

1 J.-N. Chazalviel, *Phys. Rev. A: At., Mol., Opt. Phys.*, 1990, **42**, 7355–7367.

2 X.-B. Cheng, R. Zhang, C.-Z. Zhao and Q. Zhang, *Chem. Rev.*, 2017, **117**, 10403–10473.

3 J. B. Goodenough and K.-S. Park, *J. Am. Chem. Soc.*, 2013, **135**, 1167–1176.

4 D. Lin, Y. Liu and Y. Cui, *Nat. Nanotechnol.*, 2017, **12**, 194–206.

5 W. Xu, J. Wang, F. Ding, X. Chen, E. Nasybulin, Y. Zhang and J.-G. Zhang, *Energy Environ. Sci.*, 2014, **7**, 513–537.

6 F. Ding, W. Xu, X. Chen, J. Zhang, M. H. Engelhard, Y. Zhang, B. R. Johnson, J. V. Crum, T. A. Blake, X. Liu and J.-G. Zhang, *J. Electrochem. Soc.*, 2013, **160**, A1894–A1901.

7 C. Huang, J. Xiao, Y. Shao, J. Zheng, W. D. Bennett, D. Lu, L. V. Saraf, M. Engelhard, L. Ji, J. Zhang, X. Li, G. L. Graff and J. Liu, *Nat. Commun.*, 2014, **5**, 3015.

8 G. Jiang, F. Li, H. Wang, M. Wu, S. Qi, X. Liu, S. Yang and J. Ma, *Small Struct.*, 2021, **2**, 2000122.

9 K. Qin, K. Holguin, M. Mohammadiroudbari, J. Huang, E. Y. S. Kim, R. Hall and C. Luo, *Adv. Funct. Mater.*, 2021, **31**, 2009694.

10 F. Shi, A. Pei, D. T. Boyle, J. Xie, X. Yu, X. Zhang and Y. Cui, *Proc. Natl. Acad. Sci. U. S. A.*, 2018, **115**, 8529–8534.

11 Q. Wang, Z. Yao, C. Zhao, T. Verhallen, D. P. Tabor, M. Liu, F. Ooms, F. Kang, A. Aspuru-Guzik, Y.-S. Hu, M. Wagemaker and B. Li, *Nat. Commun.*, 2020, **11**, 4188.

12 S. Chen, J. Zheng, D. Mei, K. S. Han, M. H. Engelhard, W. Zhao, W. Xu, J. Liu and J. Zhang, *Adv. Mater.*, 2018, **30**, 1706102.

13 A. Mallarapu, V. S. Bharadwaj and S. Santhanagopalan, *J. Mater. Chem. A*, 2021, **9**, 4858–4869.

14 X. Ren, P. Gao, L. Zou, S. Jiao, X. Cao, X. Zhang, H. Jia, M. H. Engelhard, B. E. Matthews, H. Wu, H. Lee, C. Niu, C. Wang, B. W. Arey, J. Xiao, J. Liu, J.-G. Zhang and W. Xu, *Proc. Natl. Acad. Sci. U. S. A.*, 2020, **117**, 28603–28613.

15 Z. Yu, H. Wang, X. Kong, W. Huang, Y. Tsao, D. G. Mackanic, K. Wang, X. Wang, W. Huang, S. Choudhury, Y. Zheng, C. V. Amanchukwu, S. T. Hung, Y. Ma, E. G. Lomeli, J. Qin, Y. Cui and Z. Bao, *Nat. Energy*, 2020, **5**, 526–533.

16 S. Chen, Y. Xiang, G. Zheng, Y. Liao, F. Ren, Y. Zheng, H. He, B. Zheng, X. Liu, N. Xu, M. Luo, J. Zheng and Y. Yang, *ACS Appl. Mater. Interfaces*, 2020, **12**, 27794–27802.

17 J. Qian, W. A. Henderson, W. Xu, P. Bhattacharya, M. Engelhard, O. Borodin and J.-G. Zhang, *Nat. Commun.*, 2015, **6**, 6362.

18 X. Ren, S. Chen, H. Lee, D. Mei, M. H. Engelhard, S. D. Burton, W. Zhao, J. Zheng, Q. Li, M. S. Ding, M. Schroeder, J. Alvarado, K. Xu, Y. S. Meng, J. Liu, J.-G. Zhang and W. Xu, *Chem.*, 2018, **4**, 1877–1892.

19 Q. Zhang, S. Liu, Y. Lu, L. Xing and W. Li, *J. Energy Chem.*, 2021, **58**, 198–206.

20 X. Cao, L. Zou, B. E. Matthews, L. Zhang, X. He, X. Ren, M. H. Engelhard, S. D. Burton, P. Z. El-Khoury, H.-S. Lim, C. Niu, H. Lee, C. Wang, B. W. Arey, C. Wang, X. Xiao, J. Liu, W. Xu and J.-G. Zhang, *Energy Storage Mater.*, 2021, **34**, 76–84.

21 X. Cao, X. Ren, L. Zou, M. H. Engelhard, W. Huang, H. Wang, B. E. Matthews, H. Lee, C. Niu, B. W. Arey, Y. Cui, C. Wang, J. Xiao, J. Liu, W. Xu and J.-G. Zhang, *Nat. Energy*, 2019, **4**, 796–805.

22 L. E. Camacho-Forero, T. W. Smith and P. B. Balbuena, *J. Phys. Chem. C*, 2017, **121**, 182–194.

23 Y. Zheng and P. B. Balbuena, *J. Chem. Phys.*, 2021, **154**, 104702.

24 T. P. Senftle, S. Hong, M. M. Islam, S. B. Kylasa, Y. Zheng, Y. K. Shin, C. Junkermeier, R. Engel-Herbert, M. J. Janik, H. M. Aktulga, T. Verstraelen, A. Grama and A. C. T. van Duin, *npj Computational Materials*, 2016, **2**, 15011.

25 M. M. Islam, G. Kolesov, T. Verstraelen, E. Kaxiras and A. C. T. van Duin, *J. Chem. Theory Comput.*, 2016, **12**, 3463–3472.

26 M. M. Islam and A. C. T. van Duin, *J. Phys. Chem. C*, 2016, **120**, 27128–27134.

27 I. Leven, H. Hao, S. Tan, X. Guan, K. A. Penrod, D. Akbarian, B. Evangelisti, M. J. Hossain, M. M. Islam, J. P. Koski, S. Moore, H. M. Aktulga, A. C. T. van Duin and T. Head-Gordon, *J. Chem. Theory Comput.*, 2021, **17**, 3237–3251.

28 Y. Liu, Q. Sun, P. Yu, Y. Wu, L. Xu, H. Yang, M. Xie, T. Cheng and W. A. Goddard, *J. Phys. Chem. Lett.*, 2021, **12**, 2922–2929.

29 Y. Liu, P. Yu, Q. Sun, Y. Wu, M. Xie, H. Yang, T. Cheng and W. A. Goddard, *ACS Energy Lett.*, 2021, **6**, 2320–2327.

30 Y. Liu, P. Yu, Y. Wu, H. Yang, M. Xie, L. Huai, W. A. Goddard and T. Cheng, *J. Phys. Chem. Lett.*, 2021, **12**, 1300–1306.

31 K. Chenoweth, A. C. T. van Duin and W. A. Goddard, *J. Phys. Chem. A*, 2008, **112**, 1040–1053.

32 J. P. Perdew, K. Burke and M. Ernzerhof, *Phys. Rev. Lett.*, 1996, **77**, 3865–3868.

33 L. Köhler and G. Kresse, *Phys. Rev. B: Condens. Matter Mater. Phys.*, 2004, **70**, 165405.

34 H. Yang, F. R. Negreiros, Q. Sun, M. Xie, L. Sementa, M. Stener, Y. Ye, A. Fortunelli, W. A. Goddard and T. Cheng, *ACS Appl. Mater. Interfaces*, 2021, **13**, 31554–31560.

35 J. Qian, A. Baskin, Z. Liu, D. Prendergast and E. J. Crumlin, *J. Chem. Phys.*, 2020, **153**, 044709.

36 H. Zhang, C. Shen, Y. Huang and Z. Liu, *Appl. Surf. Sci.*, 2021, **537**, 147983.

37 X. Ren, P. Gao, L. Zou, S. Jiao, X. Cao, X. Zhang, H. Jia, M. H. Engelhard, B. E. Matthews, H. Wu, H. Lee, C. Niu, C. Wang, B. W. Arey, J. Xiao, J. Liu, J.-G. Zhang and W. Xu, *Proc. Natl. Acad. Sci. U. S. A.*, 2020, **117**, 28603–28613.

18690 | *Phys. Chem. Chem. Phys.*, 2022, **24**, 18684–18690

This journal is © the Owner Societies 2022